IOP Publishing Phys. Med. Biol. 65 (2020) 01NT02 (9pp) https://doi.org/10.1088/1361-6560/ab5c62

Physics in Medicine & Biology

IPEM Institute of Physics and Engineering in Medicine

NOTE

The noise navigator: a surrogate for respiratory-correlated 4D-MRI for motion characterization in radiotherapy

R J M Navest[1,2,4], S Mandija[1,2], T Bruijnen[1,2], B Stemkens[1,2], R H N Tijssen[1], A Andreychenko[1,3], J J W Lagendijk[1] and C A T van den Berg[1,2]

[1] Department of Radiotherapy, University Medical Center Utrecht, Utrecht, The Netherlands
[2] Computational Imaging Group for MRI Diagnostics & Therapy, Centre for Image Sciences, University Medical Center Utrecht, Utrecht, The Netherlands
[3] Research and Practical Clinical Center of Diagnostics and Telemedicine Technologies, Department of Health Care of Moscow, Moscow, Russia
[4] Author to whom any correspondence should be addressed.

E-mail: r.j.m.navest@umcutrecht.nl

RECEIVED
1 August 2019

REVISED
12 November 2019

ACCEPTED FOR PUBLICATION
27 November 2019

PUBLISHED
13 January 2020

Keywords: respiratory motion, 4D-MRI, radiotherapy, noise navigator, thermal noise

Supplementary material for this article is available online

Abstract

Respiratory-correlated 4D-MRI can characterize respiratory-induced motion of tumors and organs-at-risk for radiotherapy treatment planning and is a necessity for image guidance of moving tumors treated on an MRI-linac. Essential for 4D-MRI generation is a robust respiratory surrogate signal.

We investigated the feasibility of the noise navigator as respiratory surrogate signal for 4D-MRI generation. The noise navigator is based on the respiratory-induced modulation of the thermal noise variance measured by the receive coils during MR acquisition and thus is inherently present and synchronized with MRI data acquisition. Additionally, the noise navigator can be combined with any rectilinear readout strategy (e.g. radial and cartesian) and is independent of MR image contrast and imaging orientation. For radiotherapy applications, the noise navigator provides a robust respiratory signal for patients scanned with an elevated coil setup. This is particularly attractive for widely used cartesian sequences where currently a non-interfering self-navigation means is lacking for MRI-based simulation and MRI-guided radiotherapy.

The feasibility of 4D-MRI generation with the noise navigator as respiratory surrogate signal was demonstrated for both cartesian and radial readout strategies in radiotherapy setup on four healthy volunteers and two radiotherapy patients on a dedicated 1.5 T MRI scanner and two radiotherapy patients on a 1.5 T MRI-linac system. Moreover, the respiratory-correlated 4D-MR images showed liver motion comparable to a reference 2D cine MRI series for the volunteers.

For 2D cartesian cine MRI acquisitions, both the noise navigator and respiratory bellows were benchmarked against an image navigator. Respiratory phase detection based on the noise navigator agreed 1.4 times better with the image navigator than the respiratory bellows did. For a 3D Stack-of-Stars acquisitions, the noise navigator was compared to radial self-navigation and a 1.7 times higher respiratory phase detection agreement was observed than for the respiratory bellows compared to radial self-navigation.

Introduction

For radiotherapy treatment planning of abdominothoracic tumors, 4D imaging is used to characterize respiratory-induced motion of tumors and organs-at-risk in order to determine the required planning target volume margins (Rosu and Hugo 2012). Traditionally, respiratory-correlated 4D imaging was mostly performed on lung using computed tomography (CT). As lung CT provides a high contrast between the tumor and background, motion assessment is feasible. 4D magnetic resonance imaging (MRI) provides better means for motion characterization of tumor sites in the thorax (e.g. mediastinal structures) and the abdomen, because

of the superior contrast between the tumor and soft tissues in MRI. Furthermore, 4D-MRI does not use ionizing radiation and can visualize the anatomy in any desired orientation, unlike 4D-CT which only allows for transversal imaging (Stemkens *et al* 2018, Paganelli *et al* 2018b). In addition to these intrinsic benefits of MRI over CT in the treatment planning stage, the availability of hybrid MRI-linac systems (Lagendijk *et al* 2014, Mutic and Dempsey 2014) for MRI-guided radiotherapy is increasing. This further increases the relevance and necessity of 4D-MRI as it is required for image guidance of moving tumors treated on an MRI-linac.

Essential for high quality respiratory-correlated 4D-MRI is an accurate retrospective sorting of the MRI data into different respiratory phases. In this manuscript we focus on 3D MRI acquisitions, as they typically have a higher signal-to-noise ratio compared to 2D MRI (Brown *et al* 2014). Furthermore, 3D imaging allows isotropic high-resolution voxels since the slice thickness is not limited by the slice excitation profile like in 2D MRI (Walton *et al* 1997) and enables geometry correction in 3D. Sorting of the raw MRI data (i.e. k-space data) is performed based on respiratory surrogate signals. There are three surrogate types, i.e. external, internal and self-navigated surrogates. External surrogate signals not based on MR signal, such as respiratory bellows (Ehman *et al* 1984, Runge *et al* 1984), are most commonly used in MRI diagnostics. In practice robust performance of these external surrogate sensors can be challenging due to various issues such as signal saturation, gain resetting, and incorrect synchronization with MRI data acquisition (Tryggestad *et al* 2013, Stemkens *et al* 2015). Moreover, external sensors lack correlation with respect to the internal anatomy (Koch *et al* 2004, Liu *et al* 2004, Feng *et al* 2009, Meschini *et al* 2019) and require additional hardware which potentially interferes with radiotherapy (e.g. body contour distortions or even modification of dose deposition). These drawbacks hamper applications for MRI-based radiotherapy simulation or on an MRI-linac. Internal surrogates rely on MRI acquisitions (e.g. pencil-beam navigators (Ehman and Felmlee 1989)) and thus decrease scanning efficiency (Buerger *et al* 2013) and can disrupt the imaging steady-state (Scheffler and Lehnhardt 2003). Contrary to external and internal surrogates, self-navigation utilizes the acquired MRI data itself to detect motion and is mostly based on non-cartesian readout strategies where the signal of the k-space center is modulated by respiration. Self-navigation does not interfere with MRI acquisition, but can suffer from potential MRI data inconsistency e.g. phase instability, eddy currents disturbing the k-space center signal (Grimm *et al* 2011), and partial saturation bands (Stemkens *et al* 2018). Advantages of self-navigation include direct synchronization with the MRI data and maximum scan efficiency.

Recently a novel self-navigation approach for respiratory motion detection was proposed, i.e. the noise navigator (Andreychenko *et al* 2017, Navest *et al* 2018). The noise navigator is based on the respiratory-induced modulation of the thermal noise variance measured by the receive coils during MRI acquisition. Unlike other self-navigation methods, the noise navigator is independent of MR signal, sequence, imaging orientation and compatible with any rectilinear readout strategy (e.g. radial and cartesian). Moreover, the noise navigator inherently yields a respiratory surrogate per readout, and thus does not require repetitive sampling of the self-navigation signal. Previous work showed that the noise navigator has an approximately ten times increased respiratory motion detection sensitivity in a measurement setup where the receive array is stationary and elevated a few centimeters above the body (see supplementary material 1 (stacks.iop.org/PMB/65/01NT02/mmedia)) compared to on-body placement (Navest *et al* 2019). This is particularly relevant for 4D-MRI in a radiotherapy setting, where the anterior receive array is placed on a coil bridge to avoid body contour deformations or distortion of surface dose deposition in the skin for a hybrid MRI-linac (Zijlema *et al* 2019). Given these advantages, we investigated the feasibility of 4D-MRI based on the noise navigator for both cartesian and radial readout strategies, in a standard radiotherapy setup. The feasibility was tested on healthy volunteers and radiotherapy patients on a dedicated 1.5 T MRI scanner and 1.5 T MRI-linac system. Additionally, quantitative motion estimation based on the 4D-MR images was evaluated.

Methods

MRI experiments

Prior to the MRI measurements written informed consent, approved by the institutional review board, was obtained. For sequence details see supplementary material 2.

MRI scanner for treatment planning

Free breathing experiments were performed on a clinical 1.5 T MRI scanner (Ingenia, Philips, Best, the Netherlands) with a flat table top for four healthy volunteers, one patient with lung cancer and one pancreatic cancer patient cancer. MR signal was measured with a 12 channel posterior array located in the table and 16 channel anterior array placed on a coil bridge a few centimeters away from the body.

For each volunteer four MRI acquisitions were performed, three were used for 4D-MRI generation and one as a reference for evaluation. For 4D-MRI generation, two fully sampled transversal 3D cartesian balanced gradient echo sequences (i.e. C1 and C2) with different isotropic voxel sizes were continuously acquired for 20 repetitions. Additionally R1, a transversal 3D T1-weighted spoiled gradient echo with golden angle Stack-of-Stars (SoS)

sampling (i.e. radial in the kx-ky plane and cartesian along the kz dimension (Peters *et al* 2000, Block *et al* 2014)) was acquired. For evaluation purposes a sagittal 2D cartesian cine MRI (i.e. C_{eval}) was continuously acquired for 120 repetitions (346 ms temporal resolution) to serve as a direct and independent respiratory motion measure. The respiratory bellows were positioned according to clinical protocol and the respiratory signal was recorded during MRI data acquisition to serve as an external, independent surrogate for respiratory motion.

Both the lung and pancreatic cancer patient were scanned with a transversal 3D SoS sequence. For the lung cancer patient, this scan was combined with contrast enhancement. The start of contrast agent (Gadovist 0.1 mmol kg^{-1}) administration was synchronized with the start of the MRI acquisition. The respiratory bellows signal was not acquired for both patients as the respiratory bellows can deform the body contour, which is undesired for radiotherapy treatment planning.

MRI-linac

To demonstrate the feasibility of the noise navigator for MRI-guided radiotherapy, one patient with liver cancer and one patient with lung cancer were scanned on a 1.5 T MRI-linac system (Unity, Elekta AB, Stockholm, Sweden) with a transversal 3D SoS acquisition. MR signal was measured with a four channel posterior array located under the table and four channel anterior array placed on a coil bridge.

Respiratory surrogate calculation

Respiratory bellows

The respiratory bellows signal was linearly interpolated to match the timing of the MRI acquisition after manual synchronization.

Image navigator

A retrospective image navigator was calculated from the sagittal 2D cine MR images. The mean (in anterior-posterior direction) was calculated over thirty adjacent lines containing lung-liver interface of each 2D cine MR image to generate an image navigator similar to a pencil-beam navigator. Subsequently, the cross-correlation was calculated between this image navigator evaluated on a reference cine MR image and the other cine MR images. In combination with the known voxel size of the 2D cine MRI acquisition, the displacement was quantified.

Self-navigator

The self-navigator was calculated from the projection profiles of the entire volume (i.e. 1D Fourier transform in the feet-head direction (kz) of the central point kx = ky = 0) as described in literature (Liu *et al* 2010, Spincemaille *et al* 2011, Feng *et al* 2016, Zhang *et al* 2016).

Noise navigator

The thermal noise variance was calculated per readout (i.e. several milliseconds temporal resolution) for each receive channel (Navest *et al* 2018). A principal component analysis was performed over the receive channels. The principal component with the largest spectral component between 0.1 and 0.5 Hz was selected and a moving average filter (hamming window with 1 s width) was applied to obtain the noise navigator.

4D-MRI reconstructions

All 4D-MR images were reconstructed by solving the following optimization problem: $\mathbf{d} = arg\min_{\mathbf{d}} ||\mathbf{F}\cdot\mathbf{C}\cdot\mathbf{d}-\mathbf{m}||_2^2 + \lambda_{TV}\,||\mathbf{TV}\cdot\mathbf{d}||_1 + \lambda_W||\mathbf{W}\cdot\mathbf{d}||_1$ (Lustig *et al* 2007). Here **F** is the (nonuniform) Fourier transform operator, **C** the coil sensitivity operator, **d** is the 3D dynamic image-series with respiratory phase dimension and **m** is the corresponding multi-coil k-space data sorted according to the respiratory phase. The measured k-space data was retrospectively sorted into ten equally sized respiratory phases using phase binning, based on the different surrogate signals to obtain **m**. **TV** is the finite difference total-variation operator in the respiratory phase dimension and **W** the wavelet transform in spatial dimension with regularization parameters λ_{TV} and λ_W respectively. The 4D MR images were reconstructed with 4D compressed sensing (Lustig *et al* 2007) using the ADMM solver in the BART toolbox (Uecker *et al* 2015) with $\lambda_{TV}/\lambda_W = 0.0075/0.005$ for the cartesian datasets and using a nonlinear conjugate gradient algorithm in Matlab (Feng *et al* 2016) with $\lambda_{TV}/\lambda_W = 0.03k_{\max}/0$ for SoS datasets.

For cartesian 4D-MRI reconstructions the data was sorted based on the noise navigator and respiratory bellows. If required, a variable phase bin width was used to ensure that each respiratory phase contained the central part of k-space, similar to Cruz *et al* (2016).

For 4D SoS reconstructions a phase correction (Moussavi *et al* 2014) was applied and subsequently the data was sorted based on the noise navigator or the self-navigator.

Respiratory surrogate evaluation

2D cartesian experiments

Both the noise navigator and respiratory bellows signal were benchmarked against an image navigator derived from 2D cartesian cine MR images (i.e. C_{eval}). We regard the image navigator as the standard, because this directly visualizes the displacement of the liver-lung interface with sufficient temporal resolution.

3D radial experiments

For the evaluation of the noise navigator and respiratory bellows in combination with a 3D SoS acquisition (i.e. R1) the self-navigator was used as benchmark. In radiotherapy, the self-navigator in combination with 3D SoS sequences has been used often for respiratory-correlated 4D-MRI generation (Rank *et al* 2017, Mickevicius and Paulson 2017, Freedman *et al* 2017).

Evaluation methods

The correlation coefficient and mean time difference at inhale and exhale between the reference method (i.e. image navigator for 2D cartesian and self-navigator for 3D SoS) and the noise navigator or respiratory bellows signal were calculated.

Respiratory phase assignment of the MRI data based on two respiratory surrogates was compared through a confusion matrix. All confusion matrices were normalized so each row added up to 100% and subsequently averaged over all volunteers.

4D-MRI displacement field evaluation

As a reference, the deformation vector fields in feet-head (FH) and anterior-posterior (AP) were calculated with optical flow (Zachiu *et al* 2015b, 2015a) on the 2D cine MRI (i.e. C_{eval}). Subsequently, the mean displacement over a region-of-interest (i.e. upper part of the liver) was calculated for all cine MR images. The reference liver displacement over a respiratory cycle was calculated as the median liver displacement at inhale minus the median liver displacement at exhale over all respiratory cycles encompassed by the 2D cine MRI. The displacement vector fields in FH and AP for the respiratory-correlated 4D-MR images (i.e. C1, C2 and R1) were also calculated with optical flow. The liver displacement was defined as the difference between exhale and inhale in the same region-of-interest used for the reference 2D cine MRI. A two-sample Kolmogorov–Smirnov test (5% significance level), with null hypothesis that the displacement observed by the reference (C_{eval}) and 4D-MRI (C1, C2 or R1) are from the same continuous distribution, was performed.

Results

Figure 1 shows the respiratory surrogate signals for the 2D cartesian cine MRI measurement C_{eval} (A) and SoS acquisition R1 (B) of a representative volunteer. Notice the gain resetting of the bellows at 28 s followed by a lower amplitude (figure 1(A)), demonstrating the low fidelity of the bellows. The green and magenta dots indicate the detected inhale and exhale respectively, whereas the green and magenta numbers show the mean time difference between the reference signal (i.e. image navigator for cartesian and self-navigator for SoS) versus the respiratory bellows and noise navigator. Notice that the mean time difference is larger for the respiratory bellows compared to the noise navigator in both exhale and inhale. Additionally, the mean correlation with the reference method over all volunteers was higher for the noise navigator than respiratory bellows. The mean correlation of the noise navigator with the image navigator (for C_{eval}) and self-navigator (for R1) was 0.88 and 0.91, respectively. The respiratory bellows had a mean correlation of 0.84 and 0.69 with the image navigator and self-navigator, respectively.

Figure 2 shows the mean phase bin agreement between the image navigator and respiratory bellows (A) or noise navigator (B) for the 2D cartesian cine MRI C_{eval}. Similarly the mean phase bin agreement over the SoS acquisition R1 between the self-navigator and respiratory bellows (C) or noise navigator (D) was calculated. Notice that all confusion matrices are mostly diagonal. Additionally, the phase bin agreement was higher around the inhale phase (i.e. phase bin 1), than exhale phase (i.e. phase bin 6) for both cartesian and SoS. The phase bin agreement between the reference and respiratory bellows was approximately 1.4 and 1.7 times lower than the phase bin agreement between the reference and noise navigator for cartesian and SoS acquisitions, respectively.

In figure 3, examples of image quality are shown for a coronal slice through the liver in exhale and inhale. Figure 3(A) shows the results from a cartesian 4D-MRI (C2) of a healthy volunteer reconstructed based on the noise navigator and respiratory bellows. Analogously, figure 3(B) shows the 4D-MRI reconstructed from the SoS acquisition (R1) of the same volunteer with noise navigator and self-navigator as respiratory surrogate. For both cases the qualitative image quality between surrogates was comparable.

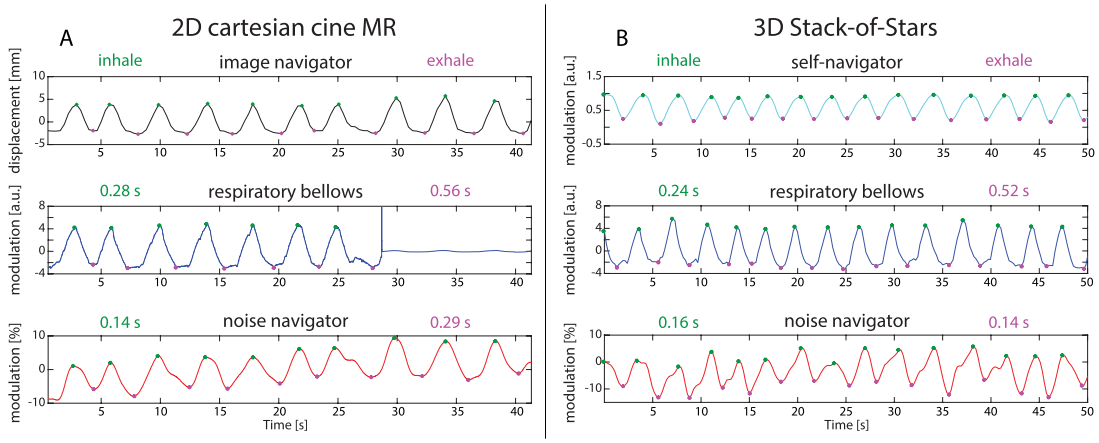

Figure 1. The image navigator, respiratory bellows and noise navigator signals for the 2D cartesian cine MR C_{eval} are shown in (A). In (B) the self-navigator, respiratory bellows and noise navigator signals are shown for the first 50 s of the SoS sequence (R1). The green and magenta dots indicate the detected inhale and exhale respectively. The green and magenta numbers indicate the mean time difference between the reference (i.e. image navigator for cartesian and self-navigator for SoS) and the respiratory bellows and noise navigator at inhale and exhale respectively.

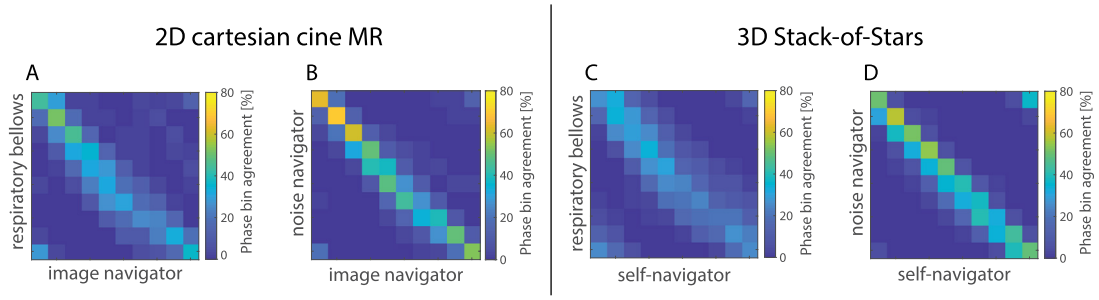

Figure 2. The phase bin agreement (in %) for the image navigator was compared to the respiratory bellows (A) and noise navigator (B). Additionally, the phase binning based on the self-navigator for the SoS acquisition was compared to the respiratory bellows (C) and noise navigator (D).

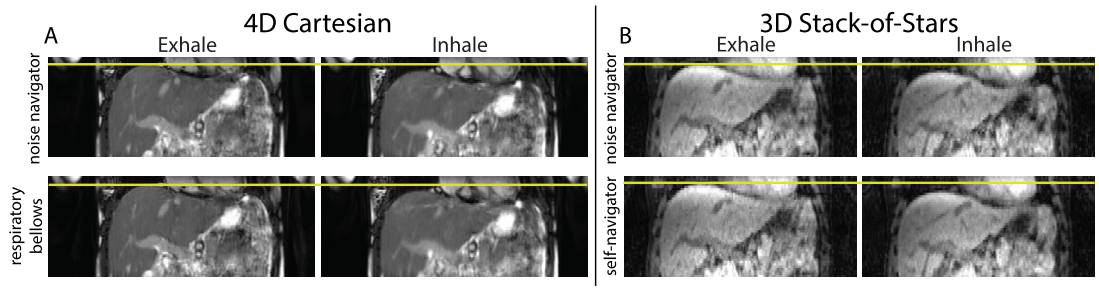

Figure 3. A coronal slice through the liver of a healthy volunteer for a balanced cartesian acquisition (C2) based on the noise navigator and respiratory bellows (A) and T1-weighted SoS acquisition (R1) based on the noise navigator and self-navigator (B). The yellow line indicates the top of the liver in exhale position.

The liver displacement calculated from the 4D-MR images was comparable for different surrogates of the same scan (see table 1). The underlined values indicate experiments where the observed 4D-MRI liver displacement was significantly different from the liver displacement measured in the 2D cine MRI.

Figure 4 shows that the image quality of the contrast enhanced 4D-MRI of a lung cancer patient acquired on the 1.5 T MRI scanner was comparable for the noise navigator and self-navigator. Moreover, the tumor (indicated by the yellow arrow) was clearly visible for both reconstructions. The animated 4D-MRI reconstructions of a lung cancer patient acquired at an MRI-linac system and pancreas cancer patient on an MRI scanner can be seen in supplementary material 3 (echo 1, 2 and 3) and 4, respectively.

Figure 5 shows the image quality improvement due to the noise navigator of the 4D-MRI generated for a patient with liver cancer on an MRI-linac system. The reconstruction based on the noise navigator showed less

Table 1. The mean liver displacement (in mm) of 4D-MRI and reference sagittal 2D cine MRI. Displacements (in mm) are reported as FH/AP. C1 and C2 indicate the first and second cartesian scan acquired per volunteer and R1 is the radial SoS. The italic displacements are significantly different from the reference displacement.

	4D Cartesian				3D Stack-of-Stars		2D Reference
	C1		C2		R1		C_{eval}
	Noise navigator	Respiratory bellows	Noise navigator	Respiratory bellows	Noise navigator	Self-navigator	
V1	10.2/2.8	8.7/2.1	7.0/1.8	6.7/1.8	6.2/1.4	7.3/1.5	8.6/2.4
V2	10.3/1.9	8.6/1.5	9.0/1.8	10.5/1.9	7.6/1.6	8.4/2.1	10.7/3.1
V3	*10.7*/2.5	*8.3*/ *1.5*	22.7/ *3.4*	24.5/3.8	20.0/ *1.9*	20.4/ *2.1*	23.5/5.2
V4	7.3/2.0	6.7/1.8	3.0/0.9	3.2/1.3	6.4/1.6	7.1/0.9	3.3/1.3

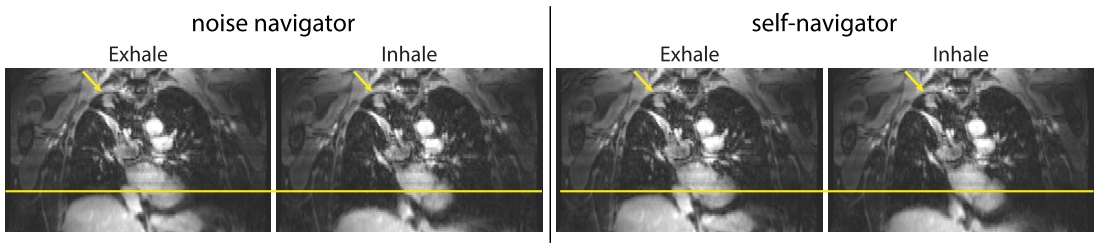

Figure 4. A coronal slice containing the lung tumor (yellow arrow) at inhale and exhale from the contrast enhanced 4D-MRI generated from a SoS sequence based on the noise navigator and self-navigator. The yellow line indicates the top of the liver in exhale position.

streaking artifacts (indicated by yellow arrows). This can be appreciated even better in the animated 4D-MRI showing all reconstructed respiratory phases in supplementary material 5.

Discussion

The feasibility of the noise navigator as a reliable respiratory surrogate for 4D-MRI generation based on 3D k-space sorting for both cartesian and radial readout strategies was shown. The largest advantage of the noise navigator is its compatibility with a wide variety of readout strategies and MR contrasts. The noise navigator, like the respiratory bellows, can be used in combination with both radial and cartesian readout strategies, whereas the self-navigator requires radial sampling for sufficient temporal resolution. Very relevant for MRI in radiotherapy, the noise navigator has a good synergy with the elevated coil setup used in radiotherapy, which augments its respiratory motion detection sensitivity significantly. The noise navigator showed a good correlation of 0.88 and 0.91 with the image navigator (for C_{eval}) and self-navigator (for R1) respectively. Both these reference methods were derived directly from the internal anatomy, and showed a higher correlation with the noise navigator than respiratory bellows. Moreover, the noise navigator provides a means of self-navigation for cartesian MRI sequences for radiotherapy simulation or even MRI-guided radiotherapy employing hybrid MRI-linacs. This is a major advantage as the respiratory bellows is unavailable at an MRI-linac system because it potentially interferes with treatment and deforms the body contour.

The 3D liver displacement could be estimated from the generated 4D-MR images (see table 1). Note that no gold standard was available for 4D-MRI displacement. Ideally, a controlled validation with a physical phantom would be performed. In practice, however, physical phantoms may not accurately depict the complex displacements observed *in vivo*. Moreover, the noise navigator depends on changes in the spatial dielectric tissue property distribution, which is most likely different for a phantom and *in vivo* making validation on a physical phantom challenging. Another potential validation method would be a digital human phantom with realistic respiratory motion (e.g. XCAT) in which realistic dielectric properties, relaxation times (i.e. T1 and T2) and proton density values are assigned to the tissues. With such a digital human phantom, the noise navigator could be calculated through electromagnetic simulations similar to Navest *et al* (2019) and the 4D-MRI sequence could be simulated similar to Paganelli *et al* (2017). If all these components were available in a single digital phantom, which is currently not the case, we believe this validation method would be valuable albeit computationally expensive. A finite-difference time-domain (FDTD) simulation would be required for the calculation of the thermal noise and separate simulations would be needed for the MR signal. Thus due to the lack of controlled validation, the optical flow derived displacement of sagittal 2D cine MRI measurements (i.e. C_{eval}), which was recorded in the same exam but not simultaneously, was used as a benchmark. The slice was positioned sagittally in order to include feet-head and anterior-posterior motion, while left-right motion was assumed to be negligibly small.

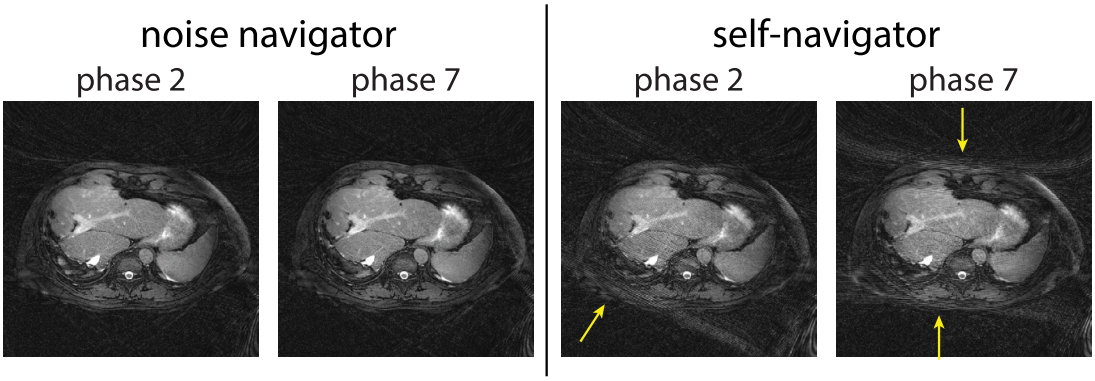

Figure 5. A transversal slice containing the liver after tumor resection at inhale and exhale. The 4D-MRI generated from a SoS sequence was based on the noise navigator and self-navigator. Notice the reduced streaking and blurring in the noise navigator based reconstruction compared to the self-navigator.

The approximately 50% FH displacement underestimation for V3 C1 with both surrogate signals was most likely caused by the blurry liver dome as a consequence of residual motion artifacts in the reconstructed inhale phase. These strong intra-bin motion artifacts are an intrinsic downside of linear phase encoded cartesian sampling and could be reduced using different profile ordering (Prieto *et al* 2015). The approximately 50% higher FH displacement for V4 C1 and V4 R1 with both surrogates was not significantly different from the reference. This was caused by the relatively large variable breathing pattern encompassed within the reference method (see supplementary material 6).

The respiratory phase binning based on the noise navigator was compared to the 2D cine MRI displacement (see figure 2(B)) and the highest agreement was observed at inhale. All surrogates showed a sharper peak at inhale than exhale, which made it easier for the peak-detection algorithm to detect inhalation than exhalation. The higher exhale detection (magenta dots) variation can be observed when comparing the image navigator and respiratory bellows between 5 and 20 s in figure 1(A). Thus the expiration time assigned by the peak-detection based on the respiratory surrogate signals is higher than one might expect from physiology. Additionally, it was observed that the noise navigator had a higher phase bin agreement with the benchmark than the respiratory bellows (see figure 2). This was partly caused by the gain resetting of the respiratory bellows signal (see figure 1(A)), which regularly occurs in a clinical setting in our experience. As a result, some respiratory cycles were not detected as such by the phase binning algorithm. This lead to wrongly assigned readouts, causing intra-bin variability and thus motion artifacts in the generated 4D-MRI.

The agreement between the noise navigator and self-navigator for 3D SoS acquisition R1 (see figure 2(D)) was lower than the observed agreement between the noise navigator and image navigator for 2D cartesian acquisition C_{eval} (see figure 2(B)). Nevertheless, 4D-MR image quality was comparable for 4D SoS reconstructions based on the noise navigator and self-navigator (see figure 3(B)). Moreover, the noise navigator could be useful in combination with dynamic contrast enhancement as this can lead to additional modulation of the radial self-navigation signal, which is based on image contrast changes (Stemkens *et al* 2019). The noise navigator does not depend on image contrast and thus is unaffected by contrast enhancement. Additionally, a rotation angle dependency in the self-navigator signal caused by direction dependent eddy currents modulating the signal at the k-space center was observed for balanced Stack-of-Stars acquisitions (Bruijnen *et al* 2019) (see supplementary material 7). This resulted in a non-uniform k-space distributions and induced streaking artifacts in the 4D-MRI reconstructed based on the self-navigator. These artifacts were largely absent in the 4D-MRI generated based on the noise navigator (see figure 5 and supplementary material 5).

In this manuscript, we focused on 4D-MRI generation based on sorting the k-space of 3D MR images. Another often used option is image-based 4D-MRI generation, where multiple 2D MR images are stitched together based on a respiratory surrogate. Since the noise navigator is insensitive to the contrast and dimensionality (i.e. 2D or 3D) of the simultaneously acquired MR images, it could in principle be used for image-based 4D-MRI generation as well. Moreover, the noise navigator could be used in synergy with image-based surrogates for 4D-MRI generation (Hui *et al* 2016, Paganelli *et al* 2018a, Meschini *et al* 2019). In addition to 4D-MRI generation, the noise navigation could be employed as independent detection means for respiration gating in MRI-guided radiotherapy. This would require a low-latency noise navigation signal (Navest *et al* 2018).

Conclusion

The feasibility of 4D-MRI generation with the noise navigator as respiratory motion surrogate has been demonstrated for both cartesian and radial readout strategies in radiotherapy setup on a dedicated 1.5 T MRI scanner and MRI-linac system for healthy volunteers and radiotherapy patients. The noise navigator provides a robust respiratory signal independent of readout strategies for patients scanned with an elevated coil setup as typically employed for radiotherapy applications. This is particularly attractive for widely employed cartesian sequences where currently a non-interfering self-navigation means is lacking for the MR based simulation and MRI-guided radiotherapy.

Acknowledgment

The authors have confirmed that any identifiable participants in this study have given their consent for publication.

ORCID iDs

R J M Navest https://orcid.org/0000-0002-0152-2092
S Mandija https://orcid.org/0000-0002-4612-5509
T Bruijnen https://orcid.org/0000-0002-1233-1320
B Stemkens https://orcid.org/0000-0003-0488-8070

References

Andreychenko A, Raaijmakers A, Sbrizzi A, Crijns S, Lagendijk J, Luijten P and van den Berg C 2017 Thermal noise variance of a receive radiofrequency coil as a respiratory motion sensor *Magn. Reson. Med.* **77** 221–8

Block K T *et al* 2014 Towards routine clinical use of radial stack-of-stars 3D gradient-Echo sequences for reducing motion sensitivity *J. Korean Soc. Magn. Reson. Med.* **18** 87

Brown R W, Cheng Y C N, Haacke E M, Thompson M R and Venkatesan R 2014 *Magnetic Resonance Imaging* 2nd edn (New York: Wiley)

Bruijnen T, Stemkens B, Lagendijk J, van den Berg C and Tijssen R 2019 Prospective GIRF-based RF phase cycling to prevent eddy current-induced steady-state disruption in balanced SSFP imaging *Proc. Int. Society for Magnetic Resonance in Medicine 27 (Montreal)* p 0762

Buerger C, Prieto C and Schaeffter T 2013 Highly efficient 3D motion-compensated abdomen MRI from undersampled golden-RPE acquisitions *Magn. Reson. Mater. Phys. Biol. Med.* **26** 419–29

Cruz G, Atkinson D, Buerger C, Schaeffter T and Prieto C 2016 Accelerated motion corrected three-dimensional abdominal MRI using total variation regularized SENSE reconstruction *Magn. Reson. Med.* **75** 1484–98

Ehman R L and Felmlee J P 1989 Adaptive technique for high-definition MR imaging of moving structures *Radiology* **173** 255–63

Ehman R L, McNamara M T, Pallack M, Hricak H and Higgins C B 1984 Magnetic resonance imaging with respiratory gating: techniques and advantages *AJR. Am. J. Roentgenol.* **143** 1175–82

Feng L, Axel L, Chandarana H, Block K T, Sodickson D K and Otazo R 2016 XD-GRASP: Golden-angle radial MRI with reconstruction of extra motion-state dimensions using compressed sensing *Magn. Reson. Med.* **75** 775–88

Feng M, Balter J M, Normolle D, Adusumilli S, Cao Y, Chenevert T L and Ben-Josef E 2009 Characterization of pancreatic tumor motion using cine MRI: surrogates for tumor position should be used with caution *Int. J. Radiat. Oncol. Biol. Phys.* **74** 884–91

Freedman J N, Collins D J, Bainbridge H, Rank C M, Nill S, Kachelrieß M, Oelfke U, Leach M O and Wetscherek A 2017 T2-Weighted 4D magnetic resonance imaging for application in magnetic resonance-guided radiotherapy treatment planning *Investigative Radiol.* **52** 563–73

Grimm R, Block K, Kiefer B and Hornegger J 2011 Bias correction for respiration detection in radial 3D gradient-Echo imaging *Proc. Int. Society for Magnetic Resonance in Medicine 19 (Montreal)* vol 19, p 2677

Hui C, Wen Z, Stemkens B, Tijssen R H N, van den Berg C A T, Hwang K P and Beddar S 2016 4D MR imaging using robust internal respiratory signal *Phys. Med. Biol.* **61** 3472–87

Koch N, Liu H, Starkschall G, Jacobson M, Forster K, Liao Z, Komaki R and Stevens C W 2004 Evaluation of internal lung motion for respiratory-gated radiotherapy using MRI: part I-correlating internal lung motion with skin fiducial motion *Int. J. Radiat. Oncol. Biol. Phys.* **60** 1459–72

Lagendijk J J, Raaymakers B W and van Vulpen M 2014 The magnetic resonance imaging-Linac system *Semin. Radiat. Oncol.* **24** 207–9

Liu H, Koch N, Starkschall G, Jacobson M, Forster K, Liao Z, Komaki R and Stevens C W 2004 Evaluation of internal lung motion for respiratory-gated radiotherapy using MRI: part II-margin reduction of internal target volume *Int. J. Radiat. Oncol. Biol. Phys.* **60** 1473–83

Liu J, Spincemaille P, Codella N C F, Nguyen T D, Prince M R and Wang Y 2010 Respiratory and cardiac self-gated free-breathing cardiac CINE imaging with multiecho 3D hybrid radial SSFP acquisition *Magn. Reson. Med.* **63** 1230–7

Lustig M, Donoho D and Pauly J M 2007 Sparse MRI: the application of compressed sensing for rapid MR imaging *Magn. Reson. Med.* **58** 1182–95

Meschini G, Paganelli C, Gianoli C, Summers P, Bellomi M, Baroni G and Riboldi M 2019 A clustering approach to 4D MRI retrospective sorting for the investigation of different surrogates *Phys. Medica* **58** 107–13

Mickevicius N J and Paulson E S 2017 Investigation of undersampling and reconstruction algorithm dependence on respiratory correlated 4D-MRI for online MR-guided radiation therapy *Phys. Med. Biol.* **62** 2910–21

Moussavi A, Untenberger M, Uecker M and Frahm J 2014 Correction of gradient-induced phase errors in radial MRI *Magn. Reson. Med.* **71** 308–12

Mutic S and Dempsey J F 2014 The ViewRay system: magnetic resonance-guided and controlled radiotherapy *Semin. Radiol. Oncol.* **24** 196–9

Navest R J M, Andreychenko A, Lagendijk J J W and van den Berg C A T 2018 Prospective respiration detection in magnetic resonance imaging by a non-interfering noise navigator *IEEE Trans. Med. Imaging* **37** 1751–60

Navest R J M, Mandija S, Andreychenko A, Raaijmakers A J E, Lagendijk J J W and Berg C A T 2019 Understanding the physical relations governing the noise navigator *Magn. Reson. Med.* **82** 2236–47

Paganelli C, Kipritidis J, Lee D, Baroni G, Keall P and Riboldi M 2018a Image-based retrospective 4D MRI in external beam radiotherapy: a comparative study with a digital phantom *Med. Phys.* **45** 3161–72

Paganelli C, Summers P, Gianoli C, Bellomi M, Baroni G and Riboldi M 2017 A tool for validating MRI-guided strategies: a digital breathing CT/MRI phantom of the abdominal site *Med. Biol. Eng. Comput.* **55** 2001–14

Paganelli C *et al* 2018b MRI-guidance for motion management in external beam radiotherapy: current status and future challenges *Phys. Med. Biol.* **63** 22TR03

Peters D C, Korosec F R, Grist T M, Block W F, Holden J E, Vigen K K and Mistretta C A 2000 Undersampled projection reconstruction applied to MR angiography *Magn. Reson. Med.* **43** 91–101

Prieto C, Doneva M, Usman M, Henningsson M, Greil G, Schaeffter T and Botnar R M 2015 Highly efficient respiratory motion compensated free-breathing coronary mra using golden-step Cartesian acquisition *J. Magn. Reson. Imaging* **41** 738–46

Rank C M, Heußer T, Buzan M T A, Wetscherek A, Freitag M T, Dinkel J and Kachelrieß M 2017 4D respiratory motion-compensated image reconstruction of free-breathing radial MR data with very high undersampling *Magn. Reson. Med.* **77** 1170–83

Rosu M and Hugo G D 2012 Advances in 4D radiation therapy for managing respiration: Part II-4D treatment planning *Z. Med. Phys.* **22** 272–80

Runge V M, Clanton J A, Partain C L and James A E 1984 Respiratory gating in magnetic resonance imaging at 0.5 Tesla *Radiology* **151** 521–3

Scheffler K and Lehnhardt S 2003 Principles and applications of balanced SSFP techniques *Eur. Radiol.* **13** 2409–18

Spincemaille P, Liu J, Nguyen T, Prince M R and Wang Y 2011 Z intensity-weighted position self-respiratory gating method for free-breathing 3D cardiac CINE imaging *Magn. Reson. Imaging* **29** 861–8

Stemkens B, Paulson E S and Tijssen R H N 2018 Nuts and bolts of 4D-MRI for radiotherapy *Phys. Med. Biol.* **63** 21TR01

Stemkens B, Prins F M, Bruijnen T, Kerkmeijer L G W, Lagendijk J J W, van den Berg C A T and Tijssen R H N 2019 A dual-purpose MRI acquisition to combine 4D-MRI and dynamic contrast-enhanced imaging for abdominal radiotherapy planning *Phys. Med. Biol.* **64** 06NT02

Stemkens B, Tijssen R H, de Senneville B D, Heerkens H D, van Vulpen M, Lagendijk J J and van den Berg C A 2015 Optimizing 4-dimensional magnetic resonance imaging data sampling for respiratory motion analysis of pancreatic tumors *Int. J. Radiat. Oncol. Biol. Phys.* **91** 571–8

Tryggestad E, Flammang A, Han-Oh S, Hales R, Herman J, McNutt T, Roland T, Shea S M and Wong J 2013 Respiration-based sorting of dynamic MRI to derive representative 4D-MRI for radiotherapy planning *Med. Phys.* **40** 051909

Uecker M, Tamir J I, Ong F and Lustig M 2015 Berkeley advanced reconstruction toolbox *Proc. Int. Society for Magnetic Resonance in Medicine 23 (Toronto)* p 2486

Walton L, Hampshire A, Forster D M and Kemeny A A 1997 Stereotactic localization with magnetic resonance imaging: a phantom study to compare the accuracy obtained using two-dimensional and three-dimensional data acquisitions *Neurosurgery* **41** 131–9

Zachiu C, Denis de Senneville B, Moonen C and Ries M 2015a A framework for the correction of slow physiological drifts during MR-guided HIFU therapies: proof of concept *Med. Phys.* **42** 4137–48

Zachiu C, Papadakis N, Ries M, Moonen C and Denis de Senneville B 2015b An improved optical flow tracking technique for real-time MR-guided beam therapies in moving organs *Phys. Med. Biol.* **60** 9003–29

Zhang T, Cheng J Y, Chen Y, Nishimura D G, Pauly J M and Vasanawala S S 2016 Robust self-navigated body MRI using dense coil arrays *Magn. Reson. Med.* **76** 197–205

Zijlema S E, Tijssen R H N, Malkov V N, van Dijk L, Hackett S L, Kok J G M, Lagendijk J J W and van den Berg C A T 2019 Design and feasibility of a flexible, on-body, high impedance coil receive array for a 1.5 T MR-linac *Phys. Med. Biol.* **64** 185004